Journal of
Materials Chemistry A

ROYAL SOCIETY
OF CHEMISTRY

PAPER

View Article Online
View Journal | View Issue

Check for updates

Cite this: *J. Mater. Chem. A*, 2022, **10**, 21044

Enhancing two-dimensional perovskite photodetector performance through balancing carrier density and directional transport†

Tao Huang,[ab] Zhicheng Zhu,[c] Chen Zhao,[ab] Wenchi Kong,[ab] Xuhang Chen,[ab] Ruiyan Li,[ab] Zhi Yu,[ab] Zhiming Shi, *[bd] Dabing Li, [bd] Bai Yang *[c] and Weili Yu *[ab]

Received 29th May 2022
Accepted 30th August 2022

DOI: 10.1039/d2ta04288f

rsc.li/materials-a

Recently, two-dimensional (2D) Ruddlesden–Popper perovskites have attracted extensive attention in the research society owing to their unique organic and inorganic layered structure induced superb stability. However, the quantum confinement effect and dielectric confinement effect caused by the layered structure of 2D perovskites limit the carrier transport and further hinder performance improvement of 2D perovskite optoelectronic devices. To resolve this problem, we have adjusted carrier density and carrier lateral transport in 2D perovskites by a layer optimization strategy. A series of 2D perovskite $PEA_2MA_{(n-1)}Pb_nI_{3n+1}$ single crystals with varying layers ($n = 1–5$) have been synthesized by an *in situ* reverse temperature crystallization procedure, and ultra-high efficiency lateral structured photodetectors have been achieved. When n is 4, the photodetector shows the highest responsivity of 3077 A W^{-1} which is over 20 times higher than previous reports. A record external quantum efficiency of $7.2 \times 10^6\%$ is also achieved. The density functional theory calculations also confirm that directional migration of perovskite carriers is optimal when the layer number of the 2D perovskite $PEA_2MA_{(n-1)}Pb_nI_{3n+1}$ is 4. This research shows that the layer number n is a key parameter in tuning the carrier density and lateral transport properties of the 2D $PEA_2MA_{(n-1)}Pb_nI_{3n+1}$ perovskite, and a balance between these two parameters can be achieved when n is 4. This work is instructive for the fabrication of high-performance 2D perovskite optoelectronic devices.

Introduction

By virtue of their excellent optical and electrical properties including high absorption coefficients,[1] direct bandgaps,[2] long carrier diffusion lengths,[3] and high carrier mobilities,[4] organic–inorganic hybrid perovskites have emerged in a variety of research fields such as solar cells,[5–7] photodetectors,[8,9] light-emitting diodes (LEDs)[10] and field effect transistors (FETs).[11] However, the conventional three-dimensional (3D) perovskite optoelectronic devices are sensitive to water and oxygen, which presents a stability challenge to their basic and applied research. 2D perovskites have shown outstanding stability in an atmospheric environment due to their unique lattice structure where the organic and inorganic components are arranged in a layered manner, which greatly broaden their application prospects. At the same time, the quantum confinement effect and dielectric confinement effect in 2D perovskites widen the bandgap and confine the vertical transport of carriers, which limits the realization of high-performance optoelectronic devices.[12,13]

Combining the advantages of 2D and 3D perovskites, quasi-2D perovskites have remarkable potential to fabricate various optoelectronic devices.[14] 2D perovskites can be described by the formula $A_2A'_{n-1}B_nX_{3n+1}$, where A represents relatively large organic monovalent cations (*e.g.*, phenethylammonium (PEA^+) and butylammonium (BA^+)), A′ represents monovalent cations (*e.g.*, methylammonium (MA^+) and formamidinium (FA^+)). B is a divalent ion such as Ge^{2+}, Sn^{2+}, or Pb^{2+}, anion X is a halide and n represents the layer number of inorganic layers between two organic layers which is closely related to the material's quantum confinement effect and dielectric confinement effect.[15] Under normal conditions, when n is 1, the structure is generally known as pure 2D perovskite, and when n is 2–5, it is considered quasi-2D perovskite. In this paper, they are collectively called 2D perovskites in the following. The specific layer-by-layer structure

---

[a] *GPL Photonic Laboratory, State Key Laboratory of Applied Optics, Changchun Institute of Optics, Fine Mechanics and Physics, Chinese Academy of Science, Changchun 130033, China. E-mail: weili.yu@ciomp.ac.cn*

[b] *University of Chinese Academy of Sciences, Beijing 100049, P. R. China*

[c] *State Key Lab of Supramolecular Structures and Materials, Jilin University, Changchun 130012, China. E-mail: byangchem@jlu.edu.cn*

[d] *State Key Laboratory of Luminescence and Applications Changchun Institute of Optics, Fine Mechanics and Physics Chinese Academy of Sciences, Changchun 130033, P. R. China. E-mail: shizm@ciomp.ac.cn*

† Electronic supplementary information (ESI) available. See **https://doi.org/10.1039/d2ta04288f**

of 2D perovskites has stimulated increasing research in photodetectors. For example, it was reported that adding DMSO to the precursor can improve the film properties and enhance the performance of the detectors.[16] Ammonium salts can also regulate the phase purity of 2D films.[17] However, how to regulate carrier density and directional transport is still less investigated.

Herein, we analyzed the carrier density and lateral transport properties of 2D perovskites. Considering that the reported 2D perovskite devices are normally based on polycrystalline thin films whose grain boundaries drastically limit the transport of carriers,[18] a layer optimization strategy has been designed and a series of 2D perovskite $PEA_2MA_{(n-1)}Pb_nI_{3n+1}$ single crystals with varying layers ($n = 1$–5) have been synthesized by an *in situ* reverse temperature crystallization procedure. The space-charge limited current (SCLC) tests show that the 2D single crystal perovskite has the highest lateral carrier mobility of 5.62×10^{-2} $cm^2\ V^{-1}\ s^{-1}$ when n is 4. The density functional theory (DFT) calculations confirmed that the most favorable condition for carrier transport appears when $n = 4$. Then lateral structure photodetectors based on single crystals with different layers are fabricated, which show the championship performance when n is 4. We find that a balance appears between the carrier density and carrier lateral transport when n is 4, which is of great significance for deepening the understanding of the working mechanism of 2D perovskites and broadening the application prospects of 2D perovskites in high-performance optoelectronic devices.

Results and discussion

Fig. 1(a) presents the schematic diagram of the lattice of $PEA_2MA_{n-1}Pb_nI_{3n+1}$ (n = 1–5) perovskites. The lead-iodine hexahedra are separated by PEA molecules in the perovskite single crystals. Fig. 1(b) illustrates the layer-number regulation effect on carriers in the 2D perovskite. With the increase of the layer number n, the bandgap of 2D perovskites gradually decreases, and the carrier density gradually increases. At the same time, with the increase of the layer number, the organic layer restriction on the carrier directional transport decreases, so a balance between the carrier density and the carrier directional transport under the transverse applied electric field may exist, as well as the lateral carrier mobility. To further explore the optical and electrical properties of materials, $PEA_2MA_{n-1}Pb_nI_{3n+1}$ single crystals with different layer numbers have been synthesized by an *in situ* inverse temperature crystallization method. As shown in Fig. S1,† 5 μl the $PEA_2MA_{n-1}Pb_nI_{3n+1}$ precursor solution was dropped onto a hydrophobic glass substrate below 100 °C, which was covered with a hydrophobic glass as shown in Fig. S2.† Then, we gradually heated it up to 120 °C till single crystals were obtained. The optical images of $PEA_2MA_{n-1}Pb_nI_{3n+1}$ single crystals are shown Fig. 1(c), from

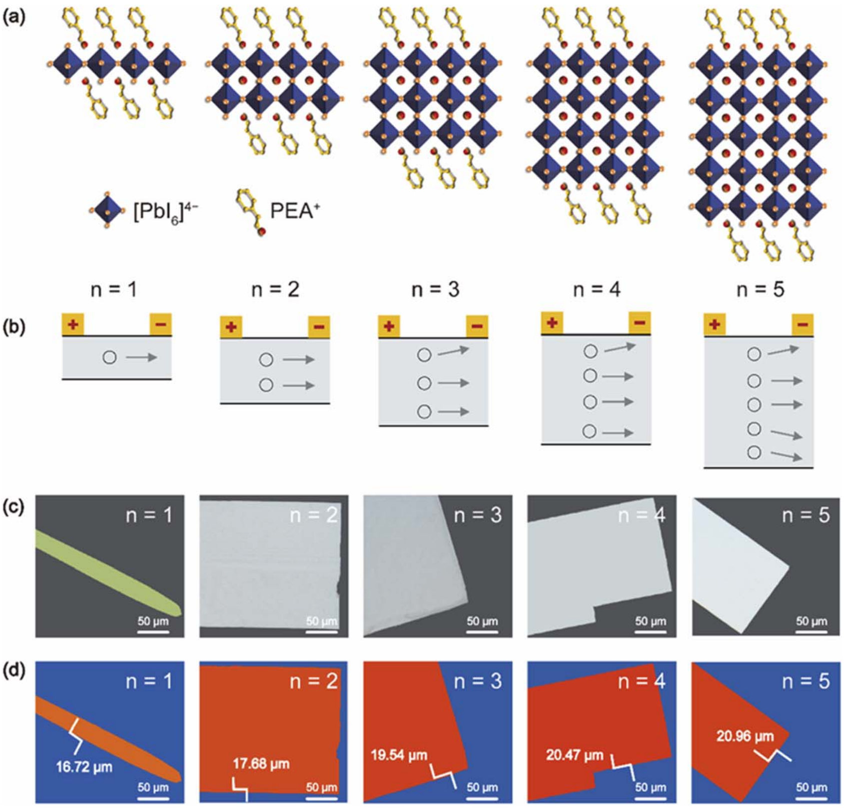

Fig. 1 (a) Schematic diagrams of the lattice of $PEA_2MA_{n-1}Pb_nI_{3n+1}$ (from left to right: $n = 1$–5) perovskites. (b) Schematic illustration of the carrier density and directional transport for different layer numbers. (c) The optical images of typical $PEA_2MA_{n-1}Pb_nI_{3n+1}$ single crystals (from left to right: $n = 1$–5). (d) Pseudo color plots of the $PEA_2MA_{n-1}Pb_nI_{3n+1}$ single crystals.

which we can infer that the surface of crystals is smooth and the edge is regular. When *n* is 1, crystals tend to be kelly-colored. As *n* increases from 2 to 5, the crystal color becomes grey. Laser confocal microscopy exposes the thickness of crystals with varying *n*, as shown in Fig. 1(d). The crystal thickness increases slightly with the layer number *n* and stabilizes at 20 μm ultimately. Roughness measurement by optical conjugate microscopy shows that the surface roughness of single crystals is in the range of 20–50 nm, which reflects the flatness of the crystal surface. To obtain more detailed 3D topography information, a 3D pseudo-color contour plot for $n = 4$ single crystals is presented in Fig. S3,† where the crystal surface and thickness distribution are more clearly presented. The energy dispersive X-ray spectroscopy (EDS) of the crystal was also carried out and the results are shown in Fig. S4,† in which the four elements including carbon (C), nitrogen (N), lead (Pb), and iodine(I) are uniformly distributed, further proving the high-quality of the crystals. High-quality crystals can effectively reduce the trap densities and recombination of carriers at defects, and the flat surface helps the perovskite to have better contact with the electrode.

To understand the influence of the layer number *n* on the perovskite single crystals' structural, optical and electrical properties, we characterized the 2D perovskite single crystals, as shown in Fig. 2. The X-ray diffraction (XRD) patterns of all crystals are demonstrated in Fig. 2(a), from which we can observe that the crystals exhibit obvious orthorhombic characteristics and it can be observed that the lattice constant gradually increases with the number of layers, especially at the (202) crystal plane.[19] In Fig. 2(b), the photoluminescence (PL) spectra of different perovskites show that the bandgap of 2D perovskites decreases as the number of layers increases and gradually becomes steady when *n* exceeds 4. All curves are normalized and excited using a 473 nm laser. When *n* is 1, 2 and 3, the peaks are centered at 530 nm, 580 nm and 620 nm, respectively. Remarkably, the PL peaks reach 743 nm and 778 nm when *n* is 4 and 5, which are close to 3D perovskite $MAPbI_3$ at 760 nm.[20] The reason for the larger *n* number 2D perovskite optical bandgap being slightly narrower than that of 3D perovskites lies in the unique quantum well structure of the 2D perovskite, which limits the electron–hole pairs to transport as excitons instead of free carriers after absorbing light.[21,22] The absorption curves in Fig. 2(c) coincide with PL curves and present obvious single crystal absorption peaks. We also measured the PL spectra and absorption spectra of 2D perovskite polycrystalline films as shown in Fig. S5.† For 2D perovskite, the band gap should be the sum of exciton binding energy and optical band gap.[23,24] Several peaks can be observed in both spectra, which indicate that polycrystalline films contain multiple components.[25] Therefore, single crystals have more advantages than polycrystalline films in component purity. Then we conducted time-resolved photoluminescence (TRPL) measurements to investigate the carrier lifetimes of all samples, as displayed in Fig. 2(d). Using the biexponential fit, the average lifetime is calculated to be 0.425 ns, 2.807 ns, 3.789 ns, 6.054 ns and 12.967 ns when *n* increases from 1 to 5, respectively. The fitting parameter details are shown in Table S1,† which indicates that the lifetime of the carrier increases with the layer number *n*. In order to analyze the carrier transfer characteristics, the SCLC measurements were conducted, as shown in Fig. S6.† The dark *I–V*

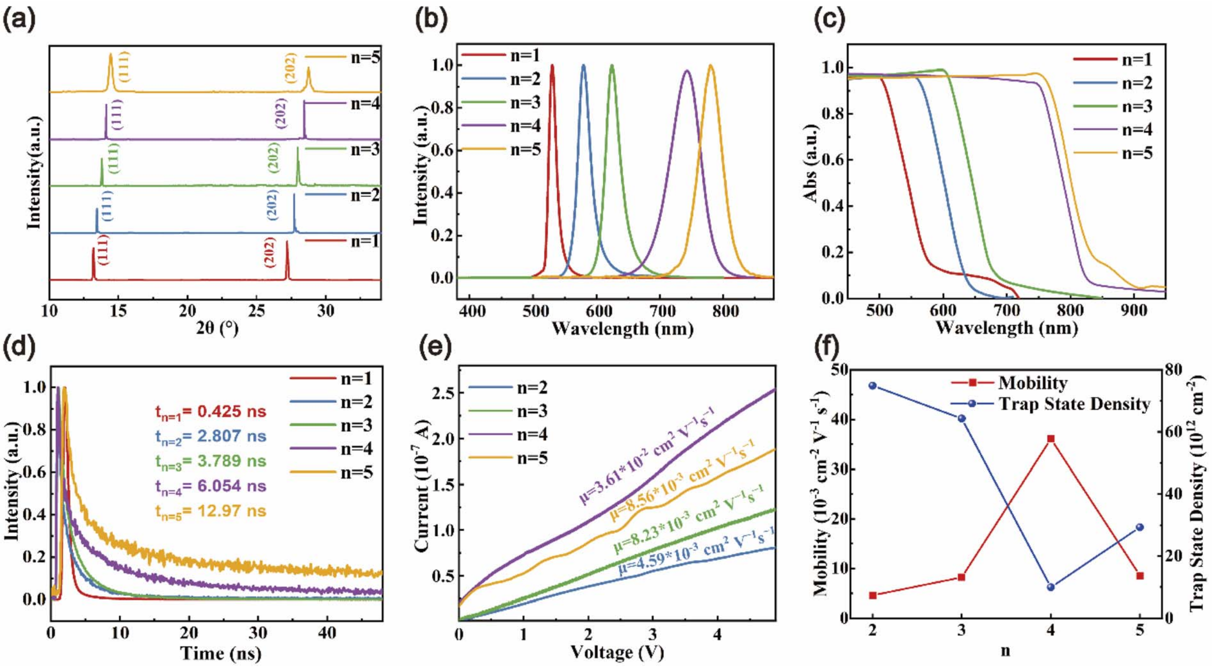

Fig. 2 (a) XRD patterns of 2D perovskite single crystals. (b) PL spectra of 2D perovskite single crystals with 473 nm laser excitation. (c) Absorption spectra of 2D perovskite single crystals. (d) TRPL spectra of 2D single crystals with 473 nm laser excitation. (e) Dark *I–V* curves of 2D perovskite single crystal devices. (f) The dependence of lateral carrier mobility and surface defect density on the layer number.

characteristics for $n = 2, 3, 4$ and 5 demonstrate the mobility of all samples, as shown in Fig. 2(e). As the injected charge carrier primarily actuates the SCLC region current, the carrier mobility is driven by:[26]

$$I = \frac{2\mu\varepsilon_0\varepsilon d}{\pi}\left(\frac{V^2}{l^2}\right) \tag{1}$$

Here, μ is the carrier mobility, ε_0 is the vacuum permittivity, ε is the relative dielectric constant of the perovskite,[27,28] and d and l are the channel width and length between the Au electrodes, respectively. The carrier mobilities for different perovskite layers from 2 to 5 are calculated to be 4.59×10^{-3} cm^2 V^{-1} s^{-1}, 8.23×10^{-3} cm^2 V^{-1} s^{-1}, 3.61×10^{-2} cm^2 V^{-1} s^{-1} and 8.56×10^{-3} cm^2 V^{-1} s^{-1}, respectively. The champion mobility appears when n is 4. As the n increases, the bandgap of 2D perovskites gradually decreases, thereby enhancing the light absorption and increasing the carrier density. In contrast, the weakening of the quantum confinement effect weakens the confinement of the direction of carrier migration. We thus believe that a balance exists between the carrier density and the quantum confinement effect that limits the directional movement of carriers.[29–32] To further verify this, PL mapping tests were carried out in all five types of perovskites, as displayed in Fig. S7.† All perovskites emit uniform PL with varying intensity. When n is 1 and 2, strong green PL can be observed. When n is greater than 2, it shows weak red PL and the PL intensity decreases significantly as the number of layers increases, and stabilizes when n exceeds 4. These results indicate that as the number of layers increases, the radiative recombination decreases and stabilizes above 4 layers, which confirms the correlation between the 2D structure and mobility from the other side. Then we calculated the trap state density (n_{trap}) of the crystal surface using the equation below:[33]

$$V_{\text{TFL}} = \frac{\pi e n_{\text{trap}} d}{4\varepsilon_0\varepsilon} \tag{2}$$

Here, V_{TFL} is trap-filled limit voltage and d is the channel width between the Au electrodes. As illustrated in Fig. S8,† the V_{TFL} of different layer perovskites from 2 to 5 is as low as 4.25 V, 2.85 V, 0.4 V and 1.05 V, and n_{trap} is computed to be 7.49×10^{13} cm^{-2}, 6.43×10^{13} cm^{-2}, 9.91×10^{12} cm^{-2} and 2.93×10^{13} cm^{-2}, respectively, which is consistent with previous reports on surface trap density.[34,35] Fig. 2(f) shows the dependence of lateral carrier mobility and surface defect density on the layer number. When n is 4, the highest lateral carrier mobility and the lowest surface defect density are achieved, which further confirms the existence of the balance point.

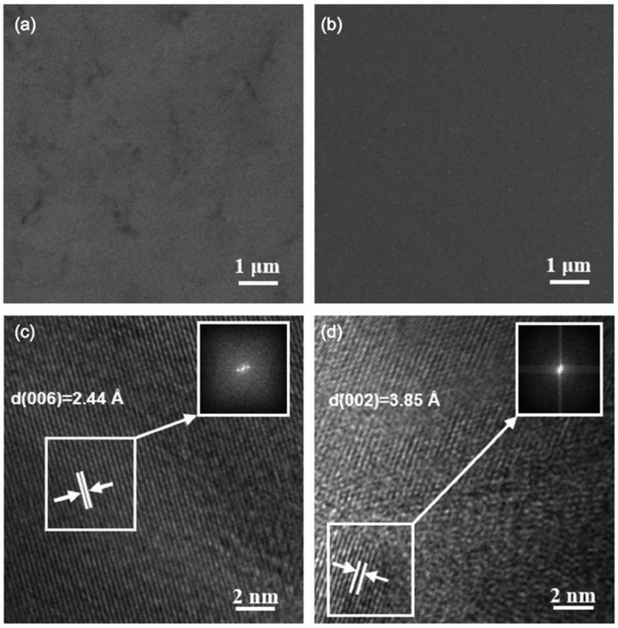

Fig. 3 SEM images of the 2D perovskite single crystal surface for (a) $n = 1$ and (b) $n = 4$, respectively. HRTEM images of the 2D perovskite single crystal surface for (c) $n = 1$ and (d) $n = 4$, respectively. The embedded images are the fast fourier transform (FFT) of the selected area.

To further characterize the surface morphology and lattice structure of 2D perovskite single crystals, we carried out high magnification scanning electron microscopy (SEM) and high-resolution transmission electron microscopy (HRTEM) characterization studies. As shown in Fig. 3(a) and (b), the surface morphology of the single crystals is smooth and free of visible defects. The SEM images of other layer perovskites are shown in Fig. S9,† which also shows the high surface flatness. In Fig. 3(c) and (d), the HRTEM images show the crystal lattice image of the single crystal when n is 1 with a lattice spacing of 2.44 Å, corresponding to the (006) crystal plane;[27] and when n is 4, the lattice spacing is 3.85 Å tallying with the (002) crystal plane. The HRTEM images for other layer perovskites are presented in Fig. S10.† It is worth noting that when n increases to 5, the lattice spacing of 3.09 Å corresponding to the (002) crystal plane of the 3D perovskite can be observed,[36] which means that as the number of layers increases, the 2D perovskite is gradually turning to 3D perovskite.

To better understand the impacts of the inorganic layer thickness on the band structure and electronic properties, DFT calculations were carried out, and the band structures of diverse layer perovskites have been demonstrated in Fig. 4. Fig. 4(a)–(e) indicate that all 2D perovskites have a direct bandgap at the G point and their bandgap gradually decreases with the increase of the layer number. The bandgaps tend to be stable when n exceeds 4, which are obviously larger than the experimental values concluded from the absorption spectra owing to exciton binding energy. The energy band information is summarized in the bandgap diagram of Fig. 4(f). We thus estimate that the exciton binding energy when n is 1–5 is 0.42 eV, 0.30 eV, 0.17 eV, 0.16 eV and 0.16 eV, respectively. It can be observed that for low-order 2D perovskites, such as when n is 1 or 2, the exciton binding energy is extremely large, and as the value of n increases, the exciton binding energy tends to be stable. This is believed due to two aspects. Firstly, as n increases, the 2D characteristics gradually decrease and approach the 3D structure, so that the quantum confinement effect gradually decreases, and the direction of carrier transmission continues to become disordered; Secondly, when n increases, the dielectric shielding

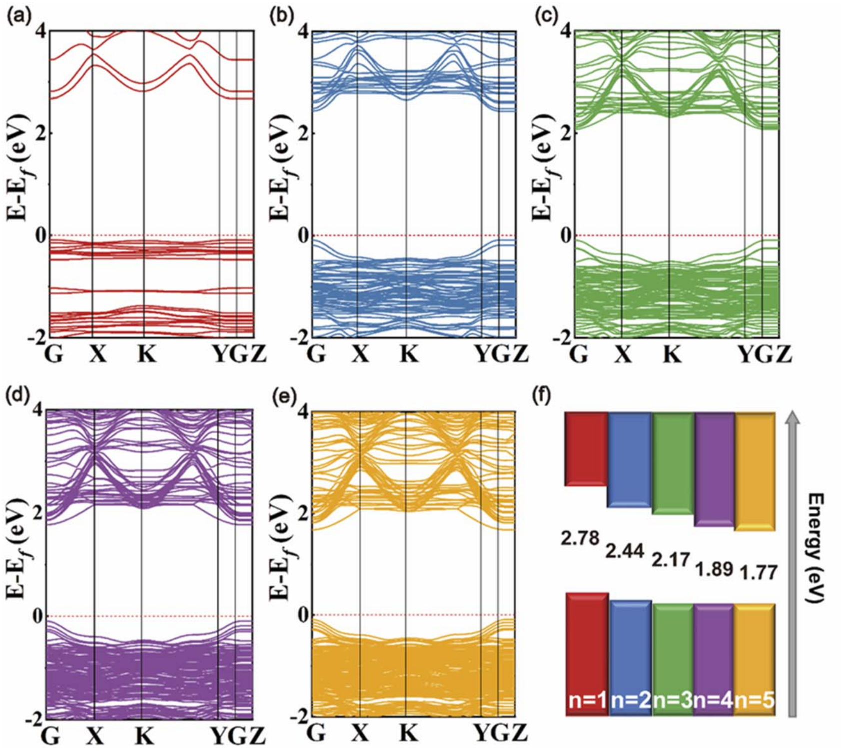

Fig. 4 (a)–(e) Band structure of 2D perovskites with varying inorganic layers from $n = 1$ to $n = 5$, respectively. The data were calculated using DFT theory. (f) Band energy diagram of $PEA_2MA_{n-1}Pb_nI_{3n+1}$ perovskite components with increasing layer number.

gradually increases. The Coulomb force between electron–hole pairs is significantly reduced, and excitons are easier to separate.[37] The bandgap values and the effective mass of holes and electrons extracted from the band structures are summarized in Table 1. All effective masses calculated from G to X points which is parallel with the perovskite inorganic layer reflect the lateral directional migration ability of carriers. The effective mass of hole increases gradually with the increase of n, representing that the lateral directional mobility of carrier gradually decreases.[38] The effective mass of electron has same trend as the hole. Regarding electron effective mass, it has the same trend as the hole effective mass. This result is beneficial for majority carrier transmission in p-type perovskites which is consistent with the larger carrier mobility when n is 4. These findings suggest that effective masses can provide a major contribution to the conductivity difference for the different layer number 2D perovskites, and has certain guiding significance for the design of devices.

Table 1 Summary of DFT calculation data for 2D perovskites

Samples	Bandgap (eV)	Electron effective mass (G–X)	Hole effective mass (G–X)
$(PEA)_2PbI_4$	2.78	0.371	0.377
$(PEA)_2(MA)_1Pb_2I_7$	2.44	0.495	0.397
$(PEA)_2(MA)_2Pb_3I_{10}$	2.17	0.567	0.399
$(PEA)_2(MA)_3Pb_4I_{13}$	1.89	0.787	0.412
$(PEA)_2(MA)_4Pb_5I_{16}$	1.77	0.801	0.463

On applying different 2D perovskites for photo detection, 2D perovskite single crystal lateral photodetectors were fabricated with the same electrode parameters of SCLC tests. The experiments were carried out under the illumination of a 532 nm laser as shown in Fig. 5(a). Both linear and saturated regions can be observed in the I–V curves of all crystals and notable light response can be detected except for n is 1, which is limited by the bandgap as the $n = 1$ sample can barely absorb 532 nm laser light. When n is 4, the largest photocurrent is achieved, and the I–V curves are shown in Fig. 5(b). For other 4 layers, the I–V curves are presented in Fig. S11.† The photocurrents of the corresponding devices *versus* light intensity are displayed in Fig. S12.† In double exponential coordinates, the α value of 0.78 when n is 4 is the optimum among all layers.

To characterize the performance of photodetectors, three key parameters including responsivity (R), external quantum efficiency (EQE), and detectivity (D) are measured. R is indicated as photocurrent generated under the stimulation of unit light intensity in unit area which can be derived from the following equation:[39]

$$R = \frac{I_{\text{light}} - I_{\text{dark}}}{P_{\text{in}} A} \tag{3}$$

Here, I_{light}, I_{dark}, P_{in} and A are photocurrent, dark current, incident optical power density and effective working area of the device, respectively. The EQE is the ratio of the number of excitation electrons *versus* incident photons as shown below:[40]

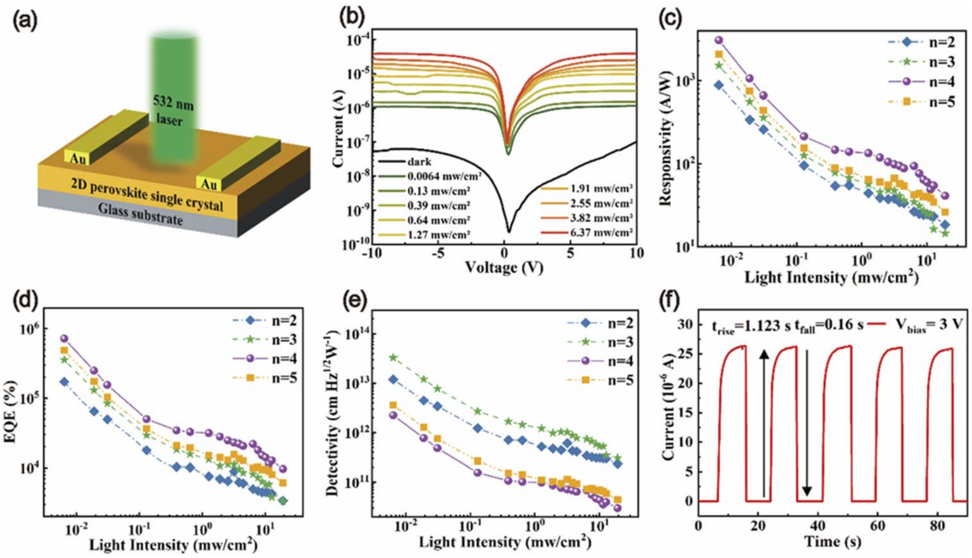

Fig. 5 (a) Schematic illustration of the photodetector architecture. (b) The *I*–*V* curves of the $(PEA)_2(MA)_3Pb_4I_{13}$ in the dark and under 532 nm light illumination with varying light intensities. (c) Responsivity, (d) EQE and (e) detectivity as a function of incident light intensity for $n = 2$, 3, 4 and 5, respectively. (f) Temporal photocurrent response of the $(PEA)_2(MA)_3Pb_4I_{13}$ photodetector under 3 V bias.

$$\mathrm{EQE} = \frac{Rh\nu}{e} \tag{4}$$

Here, h is the Planck's constant, e is the electron charge, and ν is the frequency of light. D is used to characterize the sensitivity of the device under various noises.[41] In our experiment environment, dark current is mainly affected by short noise and thus D is expressed as:[41]

$$D = \frac{R}{\sqrt{2eJ_{\mathrm{dark}}{}^2}} \tag{5}$$

Here, J_{dark} is the dark current density of the photodetector. Given the low bias of 3 V, the four 2D perovskites show superb properties, of which the optimality presents when n is 4, whose R, EQE and D are estimated to be 3077 A W^{-1}, 7.2×10^6% and 2.23×10^{12} Jones respectively at a light intensity of $\approx$6.4 μW cm^{-2}. When n is 2, 3 and 5, the overall performance is in the same order of magnitude as n is 4, as shown in Fig. 5(c)–(e). By contrast, in Fig. S13,† when n is 1, the performance is 5 orders of magnitude lower, which can be attributed to wide bandgap of the sample that needs higher light energy to excite.

We then tried to understand why the detector performance peaked at $n = 4$. According to previous literature reports, when the value of n is small, 2D perovskites mostly carry out lateral carrier transport, as the organic dielectric layers form quantum wells due to their strong insulating properties.[42–44] It is challenging for carriers to break the potential barrier of the quantum wells,[45] which affects photon absorption, limits carrier density and hinders carrier separation.[46] When the n value of the 2D perovskite increases gradually, the bandgap becomes narrower and the carrier density increases significantly.[47,48] At the same time, the relative isotropy of the 2D structure increases the uncertainty in the direction of carrier transport, so there is an optimal n value that balances lateral transport and carrier density. Fig. S14† shows the layer-number-dependent bandgap and hole effective mass curves. Among them, with the increase of n, the bandgap gradually decreases, which means that the perovskite will have better light absorption performance and higher carrier density; on the other hand, the effective hole mass in the plane also increases, which means that the directional mobility of the charge carrier gradually decreases. When n is 4, the balance of carrier density and carrier transport is achieved, and the carrier lateral mobility is the highest. Generally, the excellent performance of the device can be attributed to three aspects: firstly, preferable crystal quality with low surface defect density combined with *in situ* growth avoids transfer of damage to crystals. Secondly, the large effective electron mass results in less recombination of main carriers. Thirdly, the balance between the carrier density and the directional migration makes the lateral transport of carriers more efficient.

To verify the stability of photodetectors, light response studies have been carried out and presented in Fig. 5(f). Highly stable and repeatable response to incident light was observed, during which the time dependent response demonstrates a switch ratio $\approx$6500. The sharp rising and falling edges corresponds to the risetime and decay time of 1.12 and 0.16 s, respectively. Other layer photodetectors' temporal photocurrent responses are demonstrated in Fig. S15.† The on-off ratios are calculated to be 375, 4080, 5190 and 2200, respectively. The performance stability of the $(PEA)_2(MA)_3Pb_4I_{13}$ single crystal photodetector is determined, as shown in Fig. S16,† and it maintains 90.5% of the initial performance after 30 days in the ambient environment. The stability of the $(PEA)_2(MA)_3Pb_4I_{13}$ single crystal is guaranteed, and it is possible to improve the practicability of perovskite devices in the future. Our lateral detectors exhibited state-of-the-art photoresponsivity as high as 3077 A W^{-1} which is the highest value ever reported for 2D perovskite single crystal detectors, and surpasses the majority of 3D perovskite devices which have moderate stability. The detailed comparison of performance parameters with previously reported 2D perovskite photodetectors is summarized in Table S2.† Compared with the previous reports, our single-crystal 2D perovskite detectors show significant improvement in *R* and EQE, indicating the significance of the synthesis method and that the layer number optimization strategy is competitive for high-performance detector fabrication.

Methods

Chemicals

GBL (99%) was purchased from Aladdin Reagent Ltd. Methylammonium iodide (MAI, 99%), phenylethylammonium iodide (PEAI, 99%), and lead iodide (PbI_2, 99%) were purchased from Xi'an Polymer Light Technology Corp. All the chemicals were used as received without further purification.

Synthesis of 2D single crystals

The solvent we used is gamma-butyrolactone (GBL) and the concentration of all solutions we used is 1.2 mol L^{-1}. The substrates (glass) were cleaned successively with deionized water, ethanol, acetone, and isopropanol for 5 minutes individually by ultrasonication. After being dried in a drying box at 100 °C, the substrate and the covering glass were placed in UV–O_3 for hydrophilic treatment. Then both substrate and the covered glass were immersed in a mixed solution of hexane and octadecyltrichlorosilane (mass ratio as 600 : 1) to obtain a hydrophobic surface, and then they were rinsed with acetone for 30 s and then dried with nitrogen. A small amount (about 5 μL) of $PEA_2MA_{(n-1)}Pb_nI_{3n+1}$ precursor solution was dropped onto the glass substrate and then covered with the covering glass. Then the sandwich structure sheet was put on a hotplate, which was heated under 100 °C for 12 h, and then slowly heated to 120 °C. After 24 h, crystal growth was completed. The crystal samples should be preserved in a nitrogen environment for good stability.

Characterization

The UV-vis absorption spectra of $PEA_2MA_{(n-1)}Pb_nI_{3n+1}$ single crystals were measured with a Cary 5000 spectrophotometer from Agilent Company. PL spectra were measured with a HORIBA Scientific Raman spectrometer with 2.55 mW cm^{-2} laser intensity at 473 nm in air at room temperature. Optical images of the perovskite single crystal were obtained on a Nikon SMZ25 stereomicroscope. The thickness and roughness of the single crystal were determined using a Keyence laser confocal microscope (VK-X1000). The crystal structure was characterized by X-ray diffraction with a Bruker D8 Focus. The SEM and TEM were performed by using a Zeiss Auriga-45-06.

Hybrid lateral photodetector fabrication

To fabricate hybrid lateral photodetectors and measure SCLC, 80 nm Au electrodes with a 30 μm channel were spread evenly on the crystal surface by a thermal evaporation method. The electrodes are 35 μm wide and 180 μm long. All the *I*–*V* curves were measured at room temperature in air with a Keithley 4200A semiconductor parametric analyzer (Tektronix) and a C-100 probe station from TPSi – Company. All the photo response characteristics of the devices were measured by using a 532 nm laser with tunable light intensity from 0.0064 mW cm^{-2} to 19.11 mW cm^{-2}. The exposure time of the sample was precisely controlled using an optical shutter (VS25S2TO, UNIBLITZ) with a diameter of 2.5 mm.

DFT simulation details

First-principles calculations based on DFT were performed for the electronic structure analysis. The band structure and effective mass were calculated with the Vienna Ab Initio Simulation Package (VASP),[49] where the projector-augmented wave method was adopted. The geometry optimization was performed with the Perdew–Burke–Ernzerhof (PBE) functional.[50] An onsite interaction of 7.5 eV is considered for the Pb 6s orbital to overcome the self-interaction error. The parameter test was reported in our previous work.[51] The van der Waals interaction[52,53] is also included in the calculations in agreement with previous work.[54] We employ 0.04 and 0.03 2π/Å Γ-center *k*-grids in the structural relaxations and self-consistent calculations, respectively, and 21 *k*-points between high symmetry points of the Brillouin zone in the band structure calculations. In addition, the force and total energy convergence thresholds are set to 0.01 eV Å^{-1} and 10^{-5} eV, respectively.

Conclusions

In summary, we demonstrate there is a balance between carrier density and lateral transport of carriers in 2D $PEA_2MA_{(n-1)}Pb_nI_{3n+1}$ single crystal perovskite photodetectors. SCLC tests showed that 2D perovskites have the best lateral carrier transport ability when *n* is 4. $PEA_2MA_{(n-1)}Pb_nI_{3n+1}$ single crystal lateral photodetectors have been fabricated, and the champion device is also achieved when *n* is 4. The device exhibits a record *R* ever reported, and an ultra-high EQE which is an order of magnitude higher than previous reports. The enhanced performance signifies the layer number optimization strategy in balancing the carrier density and the horizontal transport, so as to maximize the carrier mobility and the device performance. Our study clarifies the effect of the layer number of 2D perovskites on the transport properties and device performance, and may thus provide guidance to push forward the synthesis and application of 2D perovskite single crystals in optoelectronics.

Author contributions

T. Huang and W. Yu conceived the project and designed the experiments. Z. Yu designed the device schematic and structure. T. Huang fabricated the perovskite samples and conducted the SEM, EDS, optical, XRD and absorption measurements. Z. Zhu and B. Yang conducted the HRTEM measurements and analysis. T. Huang and C. Zhao performed the TRPL measurement and analyzed the results. T. Huang, C. Zhao, W. Kong and

X. Chen performed the PL characterization and analyzed the results. T. Huang and R. Li conducted the laser confocal microscopy measurements. T. Huang and W. Kong conducted the *I–V* and the SCLC characterization studies. Z. Shi and D. Li conducted DFT calculations and analysis. Z. Shi, B. Yang and W. Yu supervised the project. T. Huang and W. Yu wrote the manuscript. All authors discussed and commented on the manuscript.

Conflicts of interest

The authors declare no conflict of interest.

Acknowledgements

This work was supported by the Natural Science Foundation of China (NSFC, 61774155 and 62121005) and K. C. Wong Education Foundation (GJTD-2018-08).

Notes and references

1 O. Malinkiewicz, A. Yella, Y. H. Lee, G. M. Espallargas, M. Graetzel, M. K. Nazeeruddin and H. J. Bolink, *Nat. Photonics*, 2014, **8**, 128.

2 J. Huang, Y. Yuan, Y. Shao and Y. Yan, *Nat. Rev. Mater.*, 2017, **2**, 17042.

3 S. D. Stranks and H. J. Snaith, *Nat. Nanotechnol.*, 2015, **10**, 391.

4 G. Xing, N. Mathews, S. Sun, S. S. Lim, Y. M. Lam, M. Grätzel, S. Mhaisalkar and T. C. Sum, *Science*, 2013, **342**, 344.

5 M. Jeong, I. W. Choi, E. M. Go, Y. Cho, M. Kim, B. Lee, S. Jeong, Y. Jo, H. W. Choi, J. Lee, J.-H. Bae, S. K. Kwak, D. S. Kim and C. Yang, *Science*, 2020, **369**, 1615.

6 C. Chang, C. Wang, R. Raja, L. Wang, C. Tsao and W. Su, *J. Mater. Chem. A*, 2018, **6**, 4179.

7 A. Younis, C. Lin, X. Guan, S. Shahrokhi, C. Huang, Y. Wang, T. He, S. Singh, L. Hu, J. R. D. Retamal, H. He Jr and T. Wu, *Adv. Mater.*, 2021, **33**, 2005000.

8 F. Li, H. Wang, D. Kufer, L. Liang, W. Yu, E. Alarousu, C. Ma, Y. Li, Z. Liu, C. Liu, N. Wei, F. Wang, L. Chen, O. F. Mohammed, A. Fratalocchi, X. Liu, G. Konstantatos and T. Wu, *Adv. Mater.*, 2017, **29**, 1602432.

9 H. Wang and D. H. Kim, *Chem. Soc. Rev.*, 2017, **46**, 5204.

10 B. Zhao, Y. Lian, L. Cui, G. Divitini, G. Kusch, E. Ruggeri, F. Auras, W. Li, D. Yang, B. Zhu, R. A. Oliver, J. L. MacManus-Driscoll, S. D. Stranks, D. Di and R. H. Friend, *Nat. Electron.*, 2020, **3**, 704.

11 W. Yu, F. Li, L. Yu, M. R. Niazi, Y. Zou, D. Corzo, A. Basu, C. Ma, S. Dey, M. L. Tietze, U. Buttner, X. Wang, Z. Wang, M. N. Hedhili, C. Guo, T. Wu and A. Amassian, *Nat. Commun.*, 2018, **9**, 5354.

12 C. R. Kagan, D. B. Mitzi and C. D. Dimitrakopoulos, *Science*, 1999, **286**, 945.

13 S. Sahayaraj, E. Radicchi, M. Ziołek, M. Scigaj, M. Tamulewicz-Szwajkowska, J. Serafinczuk, F. De Angelis and K. Wojciechowski, *J. Mater. Chem. A*, 2021, **9**, 9175.

14 I. C. Smith, E. T. Hoke, D. Solis-Ibarra, M. D. McGehee and H. I. Karunadasa, *Angew. Chem., Int. Ed.*, 2014, **53**, 11232.

15 F. Liu, L. Wang, J. Wang, F. Wang, Y. Chen, S. Zhang, H. Sun, J. Liu, G. Wang, Y. Hu and C. Jiang, *Adv. Funct. Mater.*, 2021, **31**, 2005662.

16 L. Min, W. Tian, F. Cao, J. Guo and L. Li, *Adv. Mater.*, 2021, **33**, 2101714.

17 Y. Yang, C. Liu, A. Mahata, M. Li, C. Roldán-Carmona, Y. Ding, Z. Arain, W. Xu, Y. Yang, P. A. Schouwink, A. Züttel, F. De Angelis, S. Dai and M. K. Nazeeruddin, *Energy Environ. Sci.*, 2020, **13**, 3093.

18 J. Hu, L. W. H. Oswald, S. J. Stuard, M. M. Nahid, N. Zhou, O. F. Wiliams, Z. Guo, L. Yan, H. Hu, Z. Chen, X. Xiao, Y. Lin, Z. Yang, J. Huang, A. M. Moran, H. Ade, J. R. Neilson and W. You, *Nat. Commun.*, 2019, **10**, 1276.

19 J. C. Blancon, H. Tsai, W. Nie, C. C. Stoumpos, L. Pedesseau, C. Katan, M. Kepenekian, C. M. M. Soe, K. Appavoo, M. Y. Sfeir, S. Tretiak, P. M. Ajayan, M. G. Kanatzidis, J. Even, J. J. Crochet and A. D. Mohite, *Science*, 2017, **355**, 1288.

20 Y. Lei, Y. Chen, R. Zhang, Y. Li, Q. Yan, S. Lee, Y. Yu, H. Tsai, W. Choi, K. Wang, Y. Luo, Y. Gu, X. Zheng, C. Wang, C. Wang, H. Hu, Y. Li, B. Qi, M. Lin, Z. Zhang, S. A. Dayeh, M. Pharr, D. P. Fenning, Y.-H. Lo, J. Luo, K. Yang, J. Yoo, W. Nie and S. Xu, *Nature*, 2020, **583**, 790.

21 J. C. Blancon, A. V. Stier, H. Tsai, W. Nie, C. C. Stoumpos, B. Traoré, L. Pedesseau, M. Kepenekian, F. Katsutani, G. T. Noe, J. Kono, S. Tretiak, S. A. Crooker, C. Katan, M. G. Kanatzidis, J. J. Crochet, J. Even and A. D. Mohite, *Nat. Commun.*, 2018, **9**, 2254.

22 J. C. Blancon, J. Even, C. C. Stoumpos, M. G. Kanatzidis and A. D. Mohite, *Nat. Nanotechnol.*, 2020, **15**, 969.

23 H. Tsai, R. Asadpour, J. C. Blancon, C. C. Stoumpos, J. Even, P. M. Ajayan, M. G. Kanatzidis, M. A. Alam, A. D. Mohite and W. Nie, *Nat. Commun.*, 2018, **9**, 2130.

24 L. T. Dou, A. B. Wong, Y. Yu, M. L. Lai, N. Kornienko, S. W. Eaton, A. Fu, C. G. Bischak, J. Ma, T. N. Ding, N. S. Ginsberg, L. W. Wang, A. P. Alivisatos and P. D. Yang, *Science*, 2015, **349**, 1518.

25 J. Hu, L. Yan and W. You, *Adv. Mater.*, 2018, **30**, 1802041.

26 R. Zuleeg and P. Knoll, *Appl. Phys. Lett.*, 1967, **11**, 183.

27 Y. Liu, Y. Zhang, Z. Yang, H. Ye, J. Feng, Z. Xu, X. Zhang, R. Munir, J. Liu, P. Zuo, Q. Li, M. Hu, L. Meng, K. Wang, D.-M. Smilgies, G. Zhao, H. Xu, Z. Yang, A. Amassian, J. Li, K. Zhao and S. Liu, *Nat. Commun.*, 2018, **9**, 5302.

28 S. Chen, N. Shen, L. Zhang, W. Kong, L. Zhang, C. Cheng and B. Xu, *J. Mater. Chem. A*, 2019, **7**, 9542.

29 J. Liang, Z. Zhang, Q. Xue, Y. Zheng, X. Wu, Y. Huang, X. Wang, C. Qin, Z. Chen and C. C. Chen, *Energy Environ. Sci.*, 2022, **15**, 296.

30 L. N. Quan, M. Yuan, R. Comin, O. Voznyy, E. M. Beauregard, S. Hoogland, A. Buin, A. R. Kirmani, K. Zhao, A. Amassian, D. H. Kim and E. H. Sargent, *J. Am. Chem. Soc.*, 2016, **138**, 2649.

31 J. Liu, J. Leng, K. Wu, J. Zhang and S. Jin, *J. Am. Chem. Soc.*, 2017, **139**, 1432.

32 H. Tsai, W. Nie, J.-C. Blancon, C. C. Stoumpos, R. Asadpour, B. Harutyunyan, A. J. Neukirch, R. Verduzco, J. J. Crochet, S. Tretiak, L. Pedesseau, J. Even, M. A. Alam, G. Gupta, J. Lou, P. M. Ajayan, M. J. Bedzyk, M. G. Kanatzidis and A. D. Mohite, *Nature*, 2016, **536**, 312.

33 Y. Liu, Z. Yang, D. Cui, X. Ren, J. Sun, X. Liu, J. Zhang, Q. Wei, H. Fan, F. Yu, X. Zhang, C. Zhao and S. Liu, *Adv. Mater.*, 2015, **27**, 5176.

34 J. Xing, Y. Zou, C. Zhao, Z. Yu, Y. Shan, W. Kong, X. Zheng, X. Li, W. Yu and C. Guo, *Mater. Today Phys.*, 2020, **14**, 100240.

35 J. Xing, C. Zhao, Y. Zou, W. Kong, Z. Yu, Y. Shan, Q. Dong, D. Zhou, W. Yu and C. Guo, *Light Sci. Appl.*, 2020, **9**, 111.

36 Y. Lin, Y. Fang, J. Zhao, Y. Shao, S. J. Stuard, M. M. Nahid, H. Ade, Q. Wang, J. E. Shield, N. Zhou, A. M. Moran and J. Huang, *Nat. Commun.*, 2019, **10**, 1008.

37 Y. Gao, Z. Wei, P. Yoo, E. Shi, M. Zeller, C. Zhu, P. Liao and L. Dou, *J. Am. Chem. Soc.*, 2019, **141**, 15577.

38 J. Qing, X.-K. Liu, M. Li, F. Liu, Z. Yuan, E. Tiukalova, Z. Yan, M. Duchamp, S. Chen, Y. Wang, S. Bai, J.-M. Liu, H. J. Snaith, C.-S. Lee, T. C. Sum and F. Gao, *Adv. Energy Mater.*, 2018, **8**, 1800185.

39 C. Xie, C. Mak, X. Tao and F. Yan, *Adv. Funct. Mater.*, 2017, **27**, 1603886.

40 J. Qiu, Y. Zheng, Y. Xia, L. Chao, Y. Chen and W. Huang, *Adv. Funct. Mater.*, 2019, **29**, 1806831.

41 Y. Fang, Q. Dong, Y. Shao, Y. Yuan and J. Huang, *Nat. Photonics*, 2015, **9**, 679.

42 C. Qin, T. Matsushima, W. J. Potscavage, A. S. D. Sandanayaka, M. R. Leyden, F. Bencheikh, K. Goushi, F. Mathevet, B. Heinrich, G. Yumoto, Y. Kanemitsu and C. Adachi, *Nat. Photonics*, 2020, **14**, 70.

43 C. Qin, A. S. D. Sandanayaka, C. Zhao, T. Matsushima, D. Zhang, T. Fujihara and C. Adachi, *Nature*, 2020, **585**, 53.

44 L. Min, W. Tian, F. Cao, J. Guo and L. Li, *Adv. Mater.*, 2021, **33**, 2101714.

45 Y. Xu, M. Wang, Y. Lei, Z. Ci and Z. Jin, *Adv. Energy Mater.*, 2020, **10**, 2002558.

46 J. Song, G. Zhou, W. Chen, Q. Zhang, J. Ali, Q. Hu, J. Wang, C. Wang, W. Feng, A. B. Djurišić, H. Zhu, Y. Zhang, T. Russell and F. Liu, *Adv. Mater.*, 2020, **32**, 2002784.

47 S. Kahmann, E. K. Tekelenburg, H. Duim, M. E. Kamminga and M. A. Loi, *Nat. Commun.*, 2020, **11**, 2344.

48 H. L. Loi, J. Cao, X. Guo, C.-K. Liu, N. Wang, J. Song, G. Tang, Y. Zhu and F. Yan, *Adv. Sci.*, 2020, **7**, 2000776.

49 G. García-Calderón, A. Rubio and J. Villavicencio, *Phys. Rev. A*, 1999, **59**, 1758.

50 J. P. Perdew, K. Burke and M. Ernzerhof, *Phys. Rev. Lett.*, 1997, **78**, 1396.

51 Z. Shi, Z. Cao, X. Sun, Y. Jia, D. Li, L. Cavallo and U. Schwingenschlögl, *Small*, 2019, **15**, 1900462.

52 S. Grimme, *J. Comput. Chem.*, 2006, **27**, 1787.

53 V. Barone, M. Casarin, D. Forrer, M. Pavone, M. Sambi and A. Vittadini, *J. Comput. Chem.*, 2009, **30**, 934.

54 A. M. Ganose, C. N. Savory and D. O. Scanlon, *J. Phys. Chem. Lett.*, 2015, **6**, 4594.